Control and Characterization of the Structural, Electrical, and Optical Properties of Amorphous Zinc−Indium−Tin Oxide Thin Films

D. Bruce Buchholz,[†] Jun Liu,[‡] Tobin J. Marks,[†,‡] Ming Zhang,[†] and Robert P. H. Chang*[,†]

Department of Materials Science and Engineering and the Materials Research Center and Department of Chemistry, Northwestern University, Evanston, Illinois 60208

ABSTRACT Zinc−indium−tin oxide (ZITO) films are grown by pulsed-laser deposition in which 30% of the indium in the In_2O_3 structure is replaced by substitution with zinc and tin in equal molar proportions: $In_{2-2x}Zn_xSn_xO_3$, where $x = 0.3$. Films grown at 25 and 100 °C exhibit electron diffraction patterns (EDPs) typical of amorphous materials. At a deposition temperature of 200 °C, evidence of crystallinity begins to appear in the EDP data and becomes more evident in films deposited at 400 °C. The advent of crystallinity affects the electrical properties of the ZITO film, and the effect is ascribed to the boundaries between phases in the films. The electrical and optical properties of the amorphous ZITO films grown at 25 °C are dependent on the oxygen partial pressure (P_{O_2}) during film growth, transitioning from a high-mobility (36 $cm^2/V \cdot s$) conductor ($\sigma \sim 1700$ S/cm) at $P_{O_2} = 5$ mTorr to a high-mobility semiconductor at $P_{O_2} \approx 20$ mTorr. Field-effect transistors (FETs) prepared with as-deposited amorphous ZITO channel layers on p^+-Si/300 nm SiO_2 substrates yield FETs with on/off ratios of 10^6, off currents of 10^{-8} A, and field-effect saturation mobilities of 10 $cm^2/V \cdot s$.

KEYWORDS: transparent conducting oxide • semiconductor • oxide • amorphous

INTRODUCTION

Transparent conducting oxides (TCOs) have an established record as important materials for photovoltaic devices and optoelectronic applications (1−4). More recently, transparent oxide semiconductors (TOSs) for use in thin-film transistors (TFTs) have been explored as an enabling technology for next-generation computing, communication, and identification devices (5−8). The integration of TCOs with TOSs will allow the fabrication of fully transparent electronic devices (9−12). In addition, a material that could be tailored to serve as both a TCO and a TOS would be highly desirable.

The fabrication of amorphous TCOs (a-TCOs) and amorphous TOSs (a-TOSs) is of particular interest for several reasons. In general, amorphous materials are deposited at lower temperatures than their crystalline counterparts. This would simplify deposition/manufacturing processes and expand the range of compatible substrates that the material can be deposited on, such as plastics. Amorphous materials also tend to be less prone to fracture and hence more pliable, lending themselves to the possibility of flexible electronics (6, 13−15).

Metal cations with filled d shells comprise the highest performance and most commercialized n-type TCOs. The filled d shell precludes the possibility of d → d interband transitions, which can be optically absorbing. The most prominent of the cations used in TCOs and TOSs are Zn^{2+}, Cd^{2+}, In^{3+}, and Sn^{4+} and to a lesser extent Ga^{3+} because of its relatively large band gap and the relatively poor conductivity of its oxides (16−18). The $d^{10}s^0$ conduction-band configuration of these materials also makes them ideal for amorphous electronic materials. The randomness of long-range order inherent in amorphous materials must in some way be accommodated structurally. This usually manifests itself in the relatively low energetic requirements for bond-angle bending. The anisotropic filled d shell does not typically take part in TCO bonding, which occurs primarily via the empty and isotropic s shell. If the spatial spread of the conduction s orbital is larger than the distance between cations, then the bond angle excursions should have a greatly diminished affect on the electronic properties of these materials. For this reason, Cd^{2+}, In^{3+}, Sn^{4+}, and Ga^{3+} and to a lesser extent Zn^{2+} because of the smaller spatial expanse of the conduction s orbital of a fourth-period transition metal relative to its fifth-period counterpart, are the best candidate ions for amorphous materials (8, 11, 19, 20). Careful engineering of the materials system so as to accommodate the smaller spatial expanse of the Zn^{2+} conduction s orbital, however, can render it a useful material for both a-TCO and a-TOS applications.

Indium−tin oxide (ITO) has been the industry-standard TCO because of its high conductivity and high transparency

* Corresponding author. Tel.: +1 847 491 7814. Fax: +1 847 491 4181. E-mail: r-chang@northwestern.edu.
Received for review May 12, 2009 and accepted August 31, 2009
† Department of Materials Science and Engineering and the Materials Research Center.
‡ Department of Chemistry.
DOI: 10.1021/am900321f

in the visible spectrum. Undoped indium oxide has also proved adaptable to TOS applications (21). Indium oxide is not, however, the ultimate material for all TCO and TOS applications, nor can any material be. Many device materials have chemical compatibility concerns, such as PEDOT:PSS and ITO in organic light-emitting diode and photovoltaic polymer solar cell devices (22, 23), or are performance-sensitive to electronic band alignment (24, 25). Additionally, with the ever-increasing growth of the flat-panel-display market, the indium supply has become unreliable and, thus, indium prices are subject to major instabilities (26). These concerns have provided much of the impetus to investigate new TCO and TOS materials.

The substitution of ZnO and SnO_2 in equal molar amounts (cosubstitution) for In_2O_3 has been used to create new crystalline TCO materials, $In_{2-2x}Zn_xSn_xO_3$ (27, 28). The cosubstitution of ZnO and SnO_2 creates a net-isovalent substitution pair for $2In_2O_3$, and the solid solubility of the cosubstituted pair is reported to be as high as 40% (29), which is significantly greater than when Sn, with a solid solubility of 6−7% cation in In_2O_3 (30, 31), or Zn, with a solid solubility of <1% cation in In_2O_3 (33, 34), is substituted individually. Our first studies of this material, which will be referred to as ZITO (Zn−In−Sn oxide), focused on crystalline films grown at high temperature (600−700 °C) by pulsed-laser deposition (PLD) in which 30% of In was replaced by the cosubstitution of Zn and Sn. This composition, which we call ZITO-30, was chosen because it has a large fraction of In replaced by Zn−Sn cosubstitution while maintaining a "comfortable" distance from the solid solubility limit. As might be expected, the crystalline ZITO-30 films grown at high temperature have excellent TCO properties with high conductivity and high transparency (35). However, when we grew ZITO-30 films by the same PLD technique at room temperature (25 °C), we found these films to be amorphous, as determined by electron and X-ray diffraction (XRD), but to still possess excellent properties as a TCO. We, therefore, conducted this study to investigate the properties and potential applications of ZITO-30 as an amorphous transparent electronic material (a-ZITO-30).

Our first consideration is the process window for amorphous film growth. The first part of this study examines the affect of the deposition temperature on film crystallinity, along with the attendant changes in the optical and charge-transport properties. Of particular interest is the temperature range over which amorphous films can be deposited. Our second consideration is whether a-ZITO-30 can be used as a TOS as well as a TCO material.

Several other materials that were originally developed as TCOs were subsequently modified to also serve as TOSs (36, 37). Therefore, we envisioned that a-ZITO-30 might also be rendered semiconducting and suitable for device applications as an active-element material. The electrical properties of ZITO are highly dependent on the oxygen partial pressure in the deposition ambient at the time of film growth. This is to be expected because the transport properties of many metal oxides are dependent on the concentration of uncompensated oxygen vacancies in the structure, which can serve as intrinsic donor defects, and/or the presence of oxygen interstitials, which can serve as compensating acceptor defects to donor dopants (38). The second part of this study investigates the effects of the deposition ambient on the optical and charge-transport properties of a-ZITO-30 films grown at room temperature and seeks conditions under which a-ZITO-30 is a semiconductor suitable for device application. The final section of this contribution examines the properties of field-effect TFT devices fabricated from a-ZITO-30 under deposition conditions for which the film is a semiconductor having a high carrier mobility but a low carrier concentration.

EXPERIMENTAL METHODS

Film Growth. Thin-film ZITO-30 specimens were grown by PLD from a dense hot-pressed ceramic target (25 mm diameter). The target composition was $In_{1.40}Zn_{0.33}Sn_{0.27}O_3$, or $x \sim 0.3$. PLD was accomplished with a 248 nm KrF excimer laser using a 25 ns pulse duration and operated at 2 Hz. The 200 mJ/pulse beam was focused onto a 1 mm × 2 mm spot size. The target was rotated at 5 rpm about its axis to prevent localized heating. The target−substrate separation was fixed at 8 cm. The films were grown on borosilicate−glass substrates in ambient dioxygen (O_2) in a pressure range between 0.5 and 20 mTorr. Deposition temperatures between 25 °C (room temperature) and 400 °C were investigated.

Film Analysis. The metal content of the ZITO-30 target and films was measured by energy-dispersive X-ray analysis (EDAX) using a Hitachi S4500 scanning electron microscope fitted with an Oxford Instruments INCA Energy 200 EDAX system. Multiple assays of the ZITO-30 target yielded a standard deviation of 1 atom %, and composition analysis of the films confirmed that Zn−In−Sn ratios in the as-deposited ZITO-30 films were very close to that of the original ZITO-30 target. The sheet resistance (R_s: Ω/□), carrier type, areal carrier concentration (n_a: 1/cm^2), and carrier mobility (μ_{hall}: cm^2/V · s) were measured with a Bio-Rad Microscience Hall measurement system on samples in the van der Pauw geometry. The carrier concentration (n_v: 1/cm^3) and resistivity (ρ: Ω · cm) were calculated by dividing the areal carrier concentration and sheet resistance, respectively, by the film thickness. The Hall conductivity ($\sigma_{Hall} = \sigma_0 = 1/\rho$: S/cm) was used as the direct-current conductivity. The film thickness (d: nm) was measured with a Tencor Alpha-Step P-10 profilometer over a step edge patterned with tape prior to film deposition.

The refractive indices of the films (n), at 1000 nm, were measured with a Filmetrics F20 spectral reflectometer. The optical transparency and reflectivity were measured between 250 and 2400 nm with a Perkin-Elmer Lambda 1050 fitted with a 150 mm integrating sphere that was used for both transmission and reflection measurements, in the dual-beam mode. The transmittance (T), reflectance (R), absorbance (A), absorption coefficient (α: 1/cm), and optical band gap (E_g: eV) were calculated as described in the Supporting Information.

The optical absorption data, far from the band edge, in conjunction with the Hall measurement data, were also used to calculate the free-carrier relaxation time (τ: s) and the carrier effective mass (m^*). The details of these calculations are provided in the Supporting Information. A convenient way of expressing the effective mass is as a fraction (multiple) of the electron rest mass, m^*/m_e.

Cross-sectional transmission electron microscopy (TEM) specimens were prepared using a FEI Helios 600 dual-beam focused ion beam (FIB)/scanning electron microscopy instrument instead of the standard conventional methods of slicing, polishing, dimpling, and ion milling. The FIB technique avoids the require-

ment of hot-plate heating of the samples during TEM specimen preparation. A JEM 2100 field-emission-gun (scanning) transmission electron microscope equipped with a high-angle angular-dark-field detector and an X-ray energy-dispersive spectroscopy system was used for electron diffraction patterning. Nanobeam chemical composition analysis confirmed that Zn−In−Sn ratios in the as-deposited ZITO-30 films were very close to that of the original ZITO-30 target.

Grazing-incidence XRD (GIXRD) of ZITO-30 film specimens was performed on a Rigaku ATX-G instrument at a beam incident angle of 0.5° using Ni-filtered Cu Kα radiation.

Bottom-gate ZITO-30 TFTs were fabricated on p^+-Si/SiO_2 substrates (Process Specialties, 300-nm-thick thermally grown SiO_2). The ZITO-30 films, 80 nm thick, were deposited by PLD at room temperature from the ZITO-30 target previously described. The O_2 pressure during growth was 21 mTorr. The top-contact source and drain electrodes were fabricated by depositing 50 nm of thermally evaporated Au at ~10^{-6} Torr through a shadow mask to define a channel of length (L) = 100 μm and width (W) = 2000 μm. No postdeposition processing of the film was carried out other than the room temperature deposition of the Au electrodes. The a-ZITO-30 TFTs were characterized at room temperate in air on a custom probe station with a Keithley 6430 subfemtometer and a Keithley 2400 source meter; operated by a locally written Labview program and GPIB communication. A small change in the performance was sometimes observed between the first time that a device was tested and subsequent tests; in particular, a small increase in the turn-on voltage was observed. After this small variation, the device performance remained unchanged for all subsequent tests. The values reported here are from tests performed after the initial change.

RESULTS AND DISCUSSION

Effect of the Film Deposition Temperature. A series of ZITO-30 films were grown in ambient O_2 of 5 mTorr at temperatures ranging from 25 °C (room temperature) to 400 °C. In this temperature range, the ZITO films have the same composition as the target; above ~600 °C, Zn is lost from the films unless the O_2 partial pressure of the deposition ambient is increased to >20 mTorr. To keep the interpretation of the data as straightforward as possible, the deposition temperature was maintained below 400 °C. Figure 1 shows GIXRD spectra of films grown at 25, 100, 200, and 400 °C. The films deposited at 25 and 100 °C show GIXRD typical of amorphous materials (Figure 1a,b). At 200 °C, evidence of crystallinity begins to appear (Figure 1c) and becomes more evident in the film deposited at 400 °C (Figure 1d). To confirm the ability of GIXRD to detect the onset of crystallinity, electron diffraction patterns (EDPs) were recorded from TEM samples prepared from the ZITO-30 films and are shown as insets in Figure 1. The films grown at 25 and 100 °C exhibit EDPs typical of amorphous materials (Figure 1a,b). Again at 200 °C, evidence of crystallinity begins to appear in the EPD (Figure 1c) and becomes more evident in the film deposited at 400 °C (Figure 1d). Clearly, a wide process margin for depositing a-ZITO-30 exists at room temperature.

Although the ZITO-30 films deposited between 25 and 400 °C appear to be virtually identical with the naked eye, optical absorption spectra, particularly when displayed in the manner of a Tauc plot, reveal a significant difference between the amorphous films and those that exhibit some

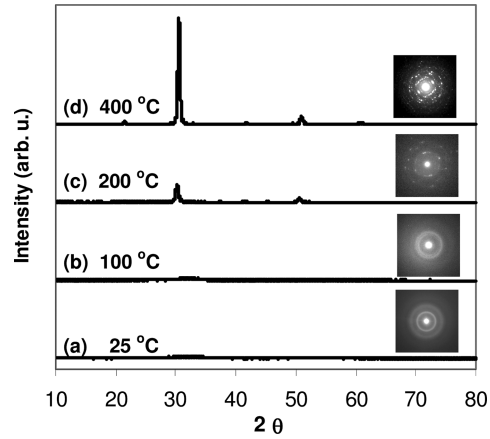

FIGURE 1. GIXRD and EDP of ZITO-30 films: (a) deposition temperature of 25 °C (amorphous); (b) deposition temperature of 100 °C (amorphous); (c) deposition temperature of 200 °C (some crystallinity evident); (d) deposition temperature of 400 °C (greater crystallinity than at 200 °C evident). The peak at ~30° corresponds to In_2O_3 (222).

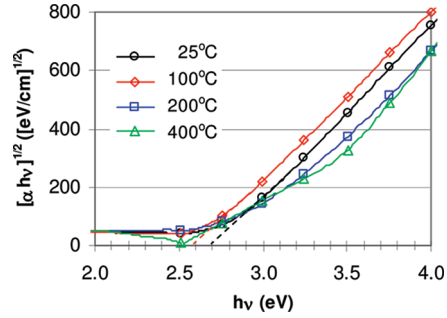

FIGURE 2. Tauc plots of ZITO-30 films as a function of the deposition temperature.

crystallinity. The optical band gap (E_g) is obtained from plots of $(\alpha h\nu)^{1/2}$ vs $h\nu$ (Figure 2). Although ZITO-30 is believed to be a direct band-gap material, an analysis by Tauc et al. concluded that for amorphous materials the Bloch functions can be described by a linear combination of the crystalline wave functions of the respective bands and, hence, the momentum, $\hbar k$, is not conserved even in a direct transition (39). Therefore, in an amorphous material, a plot of $(\alpha h\nu)^{1/2}$ vs $h\nu$ could be used to determine the band gap even for a direct transition. For the amorphous materials, the plots in Figure 2 yield a distinctly linear region with ordinate intercepts of ~2.7 eV (25 °C) and ~2.6 eV (100 °C). This is significantly less than the band gap of ~3.8 eV reported for highly crystalline ZITO-30 (40). It is, however, consistent with a weak absorption onset observed in In_2O_3 (41−43). Walsh et al. (44) have attributed the dominant optical transition in crystalline In_2O_3 at 3.75 eV to a Γ transition from a valence band ~0.8 eV below the valence band maximum (VBM) to the conduction band and the much weaker lower-energy-absorption onset to a symmetry-prohibited Γ transition from the VBM to the conduction band. In the case of an amorphous material, however, the lattice symmetry would be lost and the transition would no longer be forbidden; hence, the lower-energy transition that we observe would become the dominant one. Unlike the films that exhibit no evidence of crystallinity, the films that

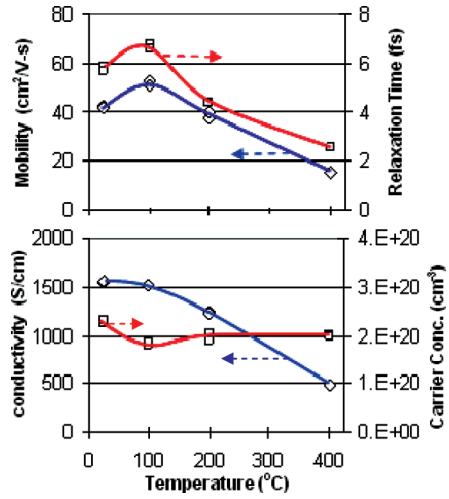

FIGURE 3. ZITO-30 film electronic-transport properties: Hall mobility (top-left axis), carrier relaxation time (top-right axis), conductivity (bottom-left axis), and carrier concentration (bottom-right axis) as a function of the deposition temperature.

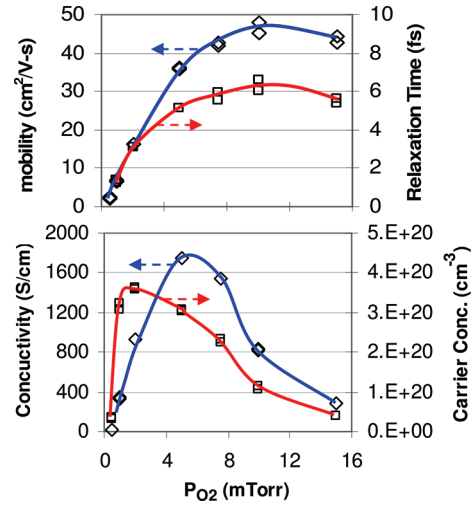

FIGURE 4. a-ZITO-30 film electronic transport properties: Hall mobility (top, left axis), carrier relaxation time (top, right axis), conductivity (bottom, left axis), and carrier concentration (bottom, right axis) as a function of the ambient film growth.

exhibit some degree of crystallinity (200 and 400 °C) do not have a single distinct linear region. This would be consistent with a material system that does not have a single phase and, hence, a single distinct absorption onset.

The degree of crystallinity also has a marked effect on the electrical and optical properties of the ZITO-30 films. The Hall mobility [μ_{Hall}; Figure 3 (top-left axis)] first increases slightly for growth temperatures between 25 and 100 °C and then decreases monotonically with increasing temperature between 100 and 400 °C. The explanation for this behavior is easiest to conceptualize in terms of the carrier relaxation time (τ). As might be expected, τ [Figure 3 (top-right axis)] closely follows the same trend as μ_{Hall}, first increasing slightly between 25 and 100 °C and then decreasing monotonically with increasing deposition temperature. The working hypothesis to explain the observed trend is scattering between regions of different structure. The monotonic decrease in τ (μ_{Hall}) with increasing deposition temperature between 100 and 400 °C is reasonably due to an increase in scattering between the crystalline and amorphous regions. As the fraction of crystalline material increases, the more likely it is that an electron will cross between the crystalline and amorphous regions. The increase in τ (μ_{Hall}) between 25 and 100 °C is speculated to be due to the relaxation of internal strains and/or the homogenization of defect concentrations (45) in the amorphous films grown at the higher temperature. Although a deposition temperature of 100 °C should not provide sufficient energy to promote crystallization, it is reasonable that the increase in the add-atom mobility over a 25 °C deposition temperature allows greater strain relaxation and defect homogenization between amorphous regions that can occur during the rapid solidification operative in a PLD process. These areas of nonuniformity scatter the electrons, hence the decrease in τ (μ_{Hall}) between the deposition temperatures of 100 and 25 °C.

The carrier concentration [n_v; Figure 3 (bottom-right axis)] varies only slightly with the growth temperature, especially when compared to the effect of the deposition ambient; see the following section. The effect of the deposition temperature on conductivity [Figure 3 (bottom-left axis)] is what might be expected from the observed carrier concentrations and mobilities, given that $\sigma = \mu n_v e$.

Although amorphous ZITO-30 films grown slightly above room temperature (100 °C) appear to have slightly better electrical transport properties, given that high carrier mobility is important for semiconductor device applications, the increase between 25 and 100 °C is modest, and for many applications, the inherent simplicity of being able to deposit at room temperature will outweigh the modest gains of substrate heating. Additionally, the lower deposition temperature will provide a process window that will help minimize the possibility that variations in other deposition parameters will induce crystallinity. Therefore, we next investigated the effects of the ambient deposition of the properties of films grown at room temperature.

Effect of the O_2 Partial Pressure. The ambient deposition, in particular, the O_2 partial pressure (P_{O_2}), can have a profound effect on the properties of oxide thin films. Room temperature depositions with P_{O_2} between 0.5 and 20 mTorr were investigated. Only the optical data for the films grown at 20 mTorr O_2 pressure will be presented because films grown at this high of a pressure are too resistive to measurement with our Hall apparatus. In particular, we seek growth conditions that yield high TCO conductivity and high transparency and also conditions that yield high TOS mobility, low carrier concentration, and high transparency.

The carrier concentration [n_v; Figure 4 (bottom-right axis)] decreases from a maximum of 3.5×10^{20} cm^{-3} at 2 mTorr O_2 with both increasing and decreasing P_{O_2}. The decrease in n_v with increasing P_{O_2} is easily explained in terms of increasing oxygen content in the film. As the O_2 pressure increases, the free-electron (carrier) concentration will decrease either by the removal of uncompensated oxygen vacancies, which can serve as intrinsic donor defects, and/or by the addition of oxygen interstitials, which can serve as compensating acceptor defects to donor dopants (38). The

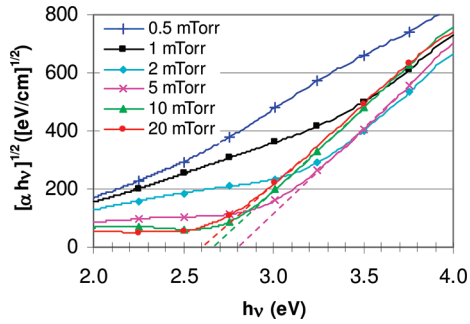

FIGURE 5. Tauc plots of a-ZITO-30 films as a function of the ambient film growth.

explanation for the decrease in n_v between 2 and 0.5 mTorr is a bit more speculative. Clearly, however, the number of donors would have to increase and/or acceptors decrease because n_v = [donors] − [acceptors] (46). It is unlikely that the number of oxygen vacancies (donors) would decrease or oxygen interstitials (acceptors) would increase as P_{O_2} is lowered. A change in the metal content could also change the ratio of donors to acceptors. However, when metal is observed to be lost (at deposition temperatures greater than 600 °C), Zn is always the metal lost. In the Zn^{2+}/Sn^{4+} substitution pair, Zn^{2+} acts as an acceptor (47); hence, the loss of Zn should result in an increase in the carriers. Another possibility would be a change (reduction) in the oxidation state of one of the metals, the most likely being Sn (48). X-ray photoelectron spectroscopy and X-ray absorption near-edge structure studies are in progress, but at present, the reason for the decrease in the carrier concentration at very low P_{O_2} remains unknown.

The Hall mobility [μ_{Hall}; Figure 4 (top-left axis)] increases as P_{O_2} increases. Again, the carrier relaxation time τ [Figure 4 (top-right axis)] closely follows the same trend as μ_{Hall}. Above P_{O_2} = 2 mTorr, the increase in τ (μ_{Hall}) is most likely due to the decrease in free electrons; because free electrons can serve as scattering sites, their removal will result in an increase in τ (μ_{Hall}). Below 2 mTorr, even with a decrease in the free electron density, τ (μ_{Hall}) decreases. One possibility is that the same defect that causes the decrease in the carrier population also disrupts the wave function, resulting in a decrease in τ (μ_{Hall}). The effect of the ambient deposition on the conductivity [Figure 4 (bottom-left axis)] is what might be expected from the observed carrier concentrations and mobilities, given that $\sigma = \mu n_v e$. The highest conductivity films, hence the most useful as TCOs, are grown at 5 mTorr. a-ZITO-30 films with low carrier concentrations but high mobilities, hence the most promising as TOSs, are grown at 15 mTorr.

The optical band gap (E_g) is obtained from Tauc plots of $(\alpha h\nu)^{1/2}$ vs $h\nu$ (Figure 5). At higher O_2 partial pressures, the plots in Figure 5 reveal a distinctly linear region with ordinate intercepts of ~2.6 eV (20 mTorr), ~2.7 eV (10 mTorr), and ~2.8 eV (5 mTorr). The decrease in the band gap between 5 and 20 mTorr is, at least in part, due to the Burstein−Moss effect (49, 50) because the trend in the carrier concentration (Figure 4) is decreasing concentration with increasing P_{O_2} above 5 mTorr. At 2 mTorr and lower, a single distinct linear

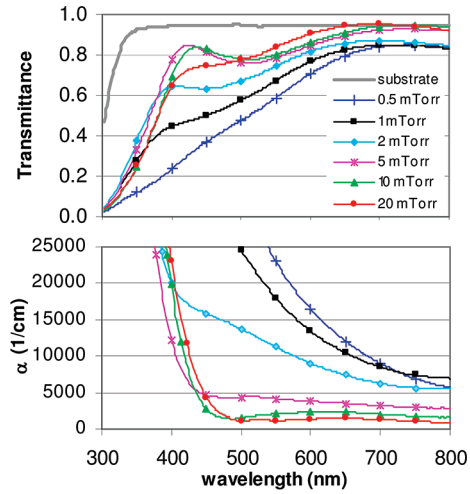

FIGURE 6. a-ZITO-30 optical absorption spectra as a function of the ambient film growth: transmittance (not corrected for reflectance), top graph; absorption coefficient (corrected for reflectance), bottom graph. All films are 160−180 nm thick.

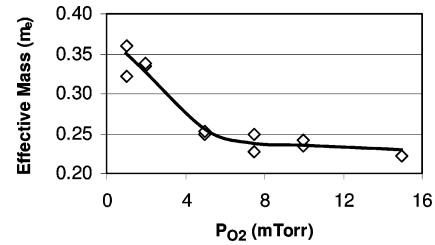

FIGURE 7. Effective carrier mass for a-ZITO-30 films as a function of the ambient growth at 25 °C.

region is not observed. This trend is qualitatively different from the loss of a single distinct linear region observed with the onset of crystallinity (Figure 2); here the nonlinear curves are shifted upward by higher absorption, whereas with the onset of crystallinity, the curves are shifted downward by lower absorptivity. The amorphous nature of these room-temperature-deposited films was verified by GIXRD (see the Supporting Information).

The transmittance of a-ZITO-30 films as a function of the wavelength and ambient deposition is shown in Figure 6; all films are between 160 and 180 nm thickness. The absorption above the band edge clearly increases as the O_2 pressure in the ambient deposition decreases. This is most easily seen in the absorbance plot where interference effects have been removed. At P_{O_2} > 5 mTorr, the decrease in the absorption with increasing pressure is most likely due to a decrease in the carrier concentration. In this pressure range, all of the films look similar to the naked eye. The films become increasingly brown to the naked eye as P_{O_2} is lowered below 5 mTorr. The increase in absorption cannot be attributed to a further increase in the carrier concentration as n_v again decreases below 2 mTorr. The exact nature of the absorption is under investigation but is likely due to changes in the band structure below 5 mTorr.

The effective mass (m^*), as calculated using the above relaxation times and the Hall mobility (see the Supporting Information), is plotted in Figure 7. At 5 mTorr and above, m^* is relatively constant, decreasing only slightly with

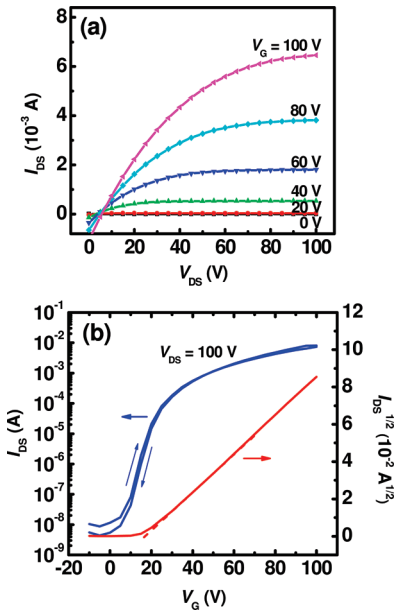

FIGURE 8. a-ZITO-30 TFT characteristics: (a) I_{DS} as a function of V_{DS} for a series of fixed gate voltages; (b) I_{DS} as a function of V_G for V_{DS} = 100 V (left axis) and $I_{DS}^{1/2}$ versus V_G for V_{DS} = 100 V (right axis).

increasing P_{O_2}. This would indicate a relatively constant band structure in this pressure range. Below 5 mTorr, there is a dramatic increase in the effective mass, indicating a significant change in the band structure.

Fortunately, as summarized earlier, the optimum electrical properties for both TCO and TOS applications occur at $P_{O_2} \geq 5$ mTorr and above, so the strong optical absorption that occurs below 5 mTorr will not affect applications using a-ZITO-30. For TCO films, a balance between the pressure where the films are the most transparent and where the films have the highest conductivity must be achieved. This is in the region of $P_{O_2} = 5-10$ mTorr. For TOS films, the electrical properties of high mobility and low carrier concentration as well as high optical transparency require a deposition P_{O_2} above 15 mTorr. Although not measurable by our Hall apparatus, a-ZITO-30 films deposited at 20 mTorr are too conductive for device applications. Only at or above 21 mTorr did the films become semiconducting enough for FET operation. The devices described in the next section were fabricated using a-ZITO-30 films grown at room temperature and P_{O_2} = 21 mTorr.

a-ZITO-30 Thin-Film Field-Effect Transistors (FETs). The combination of high carrier mobility and low carrier concentration for a-ZITO-30 films grown at high P_{O_2} makes it a good candidate for a FET material. Additionally, the PLD-derived films were quite smooth, typically having the same roughness as the substrate that they are deposited on; for Si/SiO_2, that would be 0.3−0.4 nm Ra. Bottom-gate a-ZITO-30 FETs were fabricated on p^+-Si/SiO_2 substrates. The source-drain current (I_{DS}) as a function of the source-drain voltage (V_{DS}) for a series of fixed gate voltages (V_G) is shown in Figure 8a. I_{DS} increases with V_{DS} at positive gate biases, showing that the a-ZITO-30 channel is n-type. The source-drain current as a function of the gate voltage for the fixed gate source-drain voltage of V_{DS} = 100 V is shown on the left axis of Figure 8b. The device exhibits a good FET response with a low off current, I_{off}, on the order of 10^{-8} A, and a high on-to-off source-drain current ratio, $I_{on}/I_{off} = 10^6$. Insignificant hysteresis is observed, suggesting an excellent a-ZITO-30/SiO_2 interface. The source-drain current is related to the source-drain and gate voltages by eq 1,

$$I_{DS} = C_i\mu_{FE}(V_G - V_T)^2\left(\frac{W}{2L}\right) \quad (1)$$

where C_i is the specific capacitance of the SiO_2 layer (C_i = 10 nF/cm^2), μ_{FE} is the field-effect mobility, V_T is the threshold voltage, W is the channel width, and L is the channel length (51). A plot of $I_{DS}^{1/2}$ verses V_G [Figure 8b (right axis)] will have a slope of $(C_i\mu_{FE}W/2L)^{1/2}$ from which μ_{FE} can be calculated. Extrapolation of the linear portion of the plot to the abscissa intercept is then used to determine V_T. At an operating voltage of V_{DS} = 100 V, the device has a high field-effect mobility μ_{FE} = 10 cm^2/V·s and a threshold voltage of V_T = 18 V, indicating that the TFT operates in the enhancement mode. A steep subthreshold slope of 5.5 V/decade is achieved at the maximum slope of the transfer plot. No significant difference is observed when the device is tested under light or in the dark. The amorphous ZITO-30 semiconductor shows the potential to overtake a-Si:H as a FET channel material and holds the additional potential as a channel material for transparent and flexible electronic applications.

CONCLUSIONS

While increasing the deposition temperature above 100 °C can induce crystallinity, both a-ZITO-30 TCO and TOS films can be grown at room temperature by controlling the O_2 partial pressure during the PLD process. As an amorphous TCO material, the highest conductivity for room-temperature-grown a-ZITO-30 is realized at a P_{O_2} of ∼5 mTorr, while the lowest absorption in the visible range is realized at a P_{O_2} of >10 mTorr. Therefore, a balance between the pressure where optimum optical properties occur and optimum electrical properties occur must be realized to use a-ZITO-30 as a TCO. This is in the region of P_{O_2} = 5−10 mTorr, and a-ZITO-30 TCO films are typically grown in our work at 7.5 mTorr. For an effective FET material, a combination of high transparency, high carrier mobility, and low carrier concentration is required. For a-ZITO-30, this is achieved by changing the deposition conditions to achieve a high P_{O_2}. Thin-film FETs with an a-ZITO-30 semiconducting channel layer grown at 21 mTorr exhibit high field-effect mobilities, low off currents, and high on/off ratios.

Acknowledgment. This work was supported by the Department of Energy under Grant DE-FG02-08ER46536/A000 and by the MRSEC program of the National Science Foundation under Grant NSF-DMR-0520513 at the Materials Research Center of Northwestern University. We also thank Prof. T. Mason and D. Proffit for helpful discussions on the nature of defects in bixbyite structures and for providing us with the target materials used in our experiments. The TEM specimen preparation work and EPD collection were per-

formed in the EPIC facility of the NUANCE Center at Northwestern University. The NUANCE Center is supported by NSF-NSEC, NSF-MRSEC, Keck Foundation, the State of Illinois, and Northwestern University. This work also made use of the J. B. Cohen X-ray Diffraction Facility, which is also supported by NSF-MRSEC.

Supporting Information Available: In reading manuscripts, it is sometimes unclear to me as to the methods used to distill the data. This Supporting Information provides a more detailed accounting as to the methods of data analysis. Additionally, the GIXRD data used to verify that changes in P_{O_2} did not induce crystallinity into ZITO-30 deposited at room temperature can be found here. This material is available free of charge via the Internet at http://pubs.acs.org.

REFERENCES AND NOTES

(1) Ginley, D. S.; Bright, C. *MRS Bull.* **2000**, *25*, 15–18.
(2) Minami, T.; Sonohara, H.; Kakumu, T.; Takata, S. *Jpn. J. Appl. Phys.* **1995**, *34*, L971–L974.
(3) Fortunato, E.; Ginley, D.; Hosono, H.; Paine, D. C. *MRS Bull.* **2007**, *32*, 242–247.
(4) Gorden, R. G. *MRS Bull.* **2000**, *25*, 52–57.
(5) Carcia, P. F.; McLean, R. S.; Reilly, M. H. *Appl. Phys. Lett.* **2006**, *88*, 123509-1(3).
(6) Chiang, H. Q.; Wager, J. F.; Hoffman, R. L.; Jeong, J.; Keszler, D. A. *Appl. Phys. Lett.* **2005**, *86*, 013503-1(3).
(7) Dehuff, N. L.; Kettenring, E. S.; Hong, D.; Chiang, H. Q.; Wager, J. F.; Hoffman, R. L.; Park, C.-H.; Kezler, D. A. *J. Appl. Phys.* **2005**, *97*, 064505-1(5).
(8) Barquinha, P.; Pimentel, A.; Marques, A.; Pereira, L.; Martins, R.; Fortunato, E. *J. Non-Cryst. Solids* **2006**, *352*, 1749–1752.
(9) Wagner, J. F. *Science* **2003**, *300*, 1245–1246.
(10) Fortunato, E.; Barquinha, P.; Pimentel, A.; Pereira, R.; Gonçalves, L.; Martins, R. *Phys. Status Solidi RRL* **2007**, *1*, R34–R36.
(11) Hosono, H. *Thin Solid Films* **2007**, *515*, 6000–6014.
(12) Nomura, K.; Ohta, H.; Ueda, K.; Kamiya, T.; Hirano, M.; Hosono, H. *Science* **2003**, *300*, 1269–1272.
(13) Lee, D. Y.; Lee, J. R.; Lee, G. H.; Song, P. K. *Surf. Coat. Technol.* **2008**, *202*, 5718–5723.
(14) Fortunato, E.; Barquinha, P.; Gonçalves, L.; Pereira, R.; Martins, R. *Solid-State Electron.* **2008**, *52*, 443–448.
(15) Kim, H. S.; Kim, M.-G.; Ha, Y.-G.; Kanatzidis, M. G.; Marks, T. J.; Facchetti, A. *J. Am. Chem. Soc.* **2007**, *129*, 10826–10827.
(16) Chopra, K. L.; Major, S.; Pandya, K. *Thin Solid Films* **1983**, *102*, 1–46.
(17) Freeman, A. J.; Poeppelmeier, K. R.; Mason, T. O.; Chang, R. P. H.; Marks, T. O. *MRS Bull.* **2000**, *25*, 45–51.
(18) Hartnagel, H. L.; Dawar, A. L.; Hain, A. K.; Jagadish, C. *Semiconducting Transparent Thin Films*; Institute of Physics Publishing: Bristol, U.K., 1995.
(19) Hosono, H. *J. Non-Cryst. Solids* **2006**, *352*, 851–858.
(20) Nomura, K.; Ohta, H.; Takagi, A.; Kamiya, T.; Hirano, M.; Hosono, H. *Nature* **2004**, *432*, 488–492.
(21) Wang, L.; Yoon, M.-H.; Lu, G.; Yang, Y.; Facchetti, A.; Marks, T. J. *Nat. Mater.* **2006**, *5*, 893–900.
(22) Ni, J.; Yan, H.; Wang, A.; Yang, Y.; Stern, C. L.; Metz, A. W.; Jin, S.; Wang, L.; Marks, T. J.; Ireland, J. R.; Kannewurf, C. R. *J. Am. Chem. Soc.* **2005**, *127*, 5613–5624.
(23) Sierros, K. A.; Morris, N. J.; Ramji, K.; Darran, R. C. *Thin Solid Films* **2009**, *517*, 2590–2595.
(24) Cui, J.; Wang, A. C.; Edleman, N. L.; Ni, J.; Lee, P.; Armstrong, N. R.; Marks, T. J. *Adv. Mater.* **2001**, *13*, 1476–1480.
(25) Bae, J. H.; Moon, J. M.; Jeong, S. W.; Kim, J. J.; Kang, J. W.; Kim, D. G.; Kim, J. K.; Park, J. W.; Kim, H. K. *J. Electrochem. Soc.* **2008**, *155*, J1–J6.
(26) *U.S. Department of the Interior, U.S. Geological Survey, Mineral Commodity Summaries 2009*; United States Government Printing Office: Washington, DC, 2009; pp 76—77.
(27) Palmer, G. B.; Poeppelmeier, K. R.; Mason, T. O. *Chem. Mater.* **1997**, *9*, 3121–3126.
(28) Seo, K.-H.; Lee, J.-H.; Kim, J.-J. *J. Electroceram.* **2006**, *17*, 1057–1061.
(29) Ambrosini, A.; Palmer, G. B.; Poeppelmeier, K. R.; Lane, M. A.; Brazis, P.; Kannewurf, C. R.; Hogan, T.; Mason, T. O. *Chem. Mater.* **2002**, *14*, 52–57.
(30) Enoki, H.; Echigoya, J.; Suto, H. *J. Mater. Sci.* **1991**, *26*, 4110–4115.
(31) Frank, G.; Kostlin, H. *Phys. Status Solidi* **1979**, *52*, 231–238.
(32) Frank, G.; Brock, L.; Bausen, H. *J. Cryst. Growth* **1976**, *36*, 179–180.
(33) Moriga, T.; Edwards, D. D.; Mason, T. O.; Palmer, G. B.; Poeppelmeier, K. R.; Schindler, J. L.; Kannewurf, C. R.; Nakabayashi, I. *J. Am. Ceram. Soc.* **1998**, *81*, 1310–1316.
(34) Park, D. H.; Son, K. Y.; Lee, J. H.; Kim, J. J.; Lee, J. S. *Solid State Ionics* **2004**, *172*, 431–434.
(35) Zhang, M.; Buchholz, D. B.; Xie, S. J.; Chang, R. P. H. *J. Cryst. Growth* **2007**, *308*, 376–381.
(36) Saji, K. J.; Jayaraj, M. K.; Nomura, K.; Kamiya, T.; Hosono, H. *J. Electrochem. Soc.* **2008**, *155*, H390–H395.
(37) Ogo, Y.; Nomura, K.; Yanagi, H.; Kamiya, T.; Hirano, M.; Hosono, H. *Phys. Status Solidi A* **2008**, *205*, 1920–1924.
(38) Ingram, B. J.; Gonzalez, G. B.; Kammler, D. R.; Bertoni, M. I.; Mason, T. O. *J. Electroceram.* **2004**, *13*, 167–175.
(39) Tauc, J.; Grigorovici, R.; Vancu, A. *Phys. Status Solidi* **1966**, *15*, 627–637.
(40) Harvey, S. P.; Mason, T. O.; Buchholz, D. B.; Chang, R. P. H. *J. Am. Ceram. Soc.* **2008**, *91*, 467–472.
(41) Weiher, R. L.; Ley, R. L. *J. Appl. Phys.* **1966**, *37*, 299–302.
(42) Pan, C. A.; Ma, T. P. *Appl. Phys. Lett.* **1980**, *37*, 163–165.
(43) McCann, J. F.; Bockris, J. O. M. *J. Electrochem. Soc.* **1981**, *128*, 1719–1723.
(44) Walsh, A.; Da Silva, J. L. F.; Wei, S.-H.; Kober, C.; Klein, A.; Piper, L. F. J.; DeMasi, A.; Smith, K. E.; Panaccione, G.; Torelli, P.; Payne, D. J.; Bourlange, A.; Egdell, R. G. *Phys. Rev. Lett.* **2008**, *100*, 167402-1(4).
(45) Tauc, J. *Mater. Res. Bull.* **1968**, *3*, 37–46.
(46) Harvey, S. P.; Mason, T. O.; Kober, C.; Klein, A. *Phys. Chem. Chem. Phys.* **2009**, *11*, 3099–3104.
(47) Harvey, S. P.; Poeppelmeier, K. R.; Mason, T. O. *J. Am. Ceram. Soc.* **2008**, *91*, 2683–2689.
(48) Hosono, H.; Nomura, K.; Ogo, Y.; Uruga, T.; Kamiya, T. *J. Non-Cryst. Solids* **2008**, *354*, 2796–2800.
(49) Burstein, E. *Phys. Rev.* **1954**, *93*, 632–633.
(50) Moss, T. S. *Proc. Phys. Soc. B* **1954**, *67*, 775–782.
(51) Sze, S. M. *Semiconductor Devices: Physics and Technology*; Wiley: New York, 1981.

AM900321F